Vertical profile retrievals with warm-rain microphysics using the ground-based microwave radiometer operated by the Hong Kong Observatory

Wai Soen Chan [a], Jeffrey Chi Wai Lee [b],*

[a] Department of Physics, The Chinese University of Hong Kong, Hong Kong, China
[b] Hong Kong Observatory, Hong Kong, China

ABSTRACT

We present the formulation of a variational-method-based retrieval algorithm for a ground-based microwave radiometer. Absorption by air, water vapor, cloud liquid water and rain water are incorporated into the formulation. The absorption of microwave radiation by air is calculated using a line-by-line method, while that by liquid water is calculated using an empirical formula that models the complex refractive index of liquid water. The root-mean-squared error of the retrieved temperature was no more than 1 °C in the lowest 2000 m of the profiles based on the 1-year verification data. The absorption of microwave radiation by rain water is important for improving the accuracy of the retrieval profiles during rainy conditions.

© 2015 Elsevier B.V. All rights reserved.

1. Introduction

Nowcasting of convection is a challenge. Common approaches for nowcasting include radar extrapolation (Yeung et al., 2009), dynamic numerical weather simulations (Sun et al., 2010), combined radar extrapolation and numerical simulations (Wong et al., 2009) and statistical methods (Lin et al., 2012). The last three methods are capable of forecasting the development of a convective system before it forms. However, the methods involving a numerical weather prediction system (NWP) are more computationally costly in real-time operations.

Statistical methods are limited by the available observational data. Statistical models commonly incorporate upper-air observations (Lin et al., 2011) because vertical instability is key for convective development (Adams and Souza, 2009). However, because of the operational cost, both temporal and spatial coverages of upper-air observations are insufficient to provide detailed mesoscale information for nowcasting convective development.

In recent years, real-time measurements of vertical profiles using ground-based microwave radiometers have become popular (Cimini et al., 2011; Cadeddu et al., 2013). The operational cost of ground-based microwave radiometers is much lower than that of radiosondes; thus, radiometers are more promising for improving both the spatial and temporal coverages of upper-air measurements. The accuracy of the vertical profile obtained by radiometers depends on the retrieval, which inverts the radiometer brightness temperature readings to the vertical profile. A major issue with the retrieval of vertical profiles from radiometers is that the profile during precipitation is often less accurate. This inaccuracy is caused by two effects: 1) the accumulation of water, snow (Woods et al., 2005) or ice (Fernández-González et al., 2014) over the radome and 2) the lack of scattering and emission/absorption effects of rain water in the retrieval algorithm. Attempts have been made in the past few years to solve the former problem, such as using a hydrophobic radome and forcing airflow over the radiometer surface to avoid the accumulation of water, snow and ice (Chan, 2009a) or observing the microwave irradiance at an off-zenith angle to avoid thin films of water (Xu et al., 2014). To the authors' knowledge, few attempts have been made to handle the latter problem. The two problems are distinct, but efforts devoted to solving each problem can be applied simultaneously.

There are two classes of retrieval approaches: statistical (Tan et al., 2011) and variational minimization (Hewison, 2007). The second class provides more accurate results, and it is expected to be more skillful in the application of nowcasting convective development. This article describes a vertical profile retrieval algorithm with warm-rain microphysics developed by the Hong Kong Observatory (HKO) and based on the variational minimization approach. The major objective is to address the lack of scattering and emission/absorption effects of rain water in the retrieval algorithm and the use of radar reflectivity to derive upper-air rain water content. The

impact of incorporating the scattering and emission/absorption effects of rain water is demonstrated.

2. Inputs of the retrieval algorithm

Two radiometers are operated by the HKO. One radiometer was acquired in 2008 for the Hong Kong International Airport (denoted "HKIA radiometer" hereafter), and the other radiometer was acquired in 2013 for King's Park (denoted "KP radiometer" hereafter), where the radiosonde site is located. The horizontal distance between the two radiometers is approximately 26 km. Both radiometers are 14-channel microwave radiometers (model: RPG HATPRO from Radiometer Physics, Chan (2009b)). The frequencies of the 14 channels are tabulated in Table 1. The KP radiometer was out of service for 2 months in its first year of operation. An entire calendar year of data is not available from the KP radiometer during the study period. The performance of the retrieval method was mainly tested with data from the HKIA radiometer; an exception is the analysis of the impact of incorporating rain droplet effects in the calculation, which used data from the co-sited KP radiometer. Temperature and humidity profile retrievals using the HKIA radiometer data at 0000 UTC and 1200 UTC from Sept 2010 to Aug 2011 were compared with the radiosonde data from the KP. There are 653 profiles for the comparison. We used radar reflectivity data from the S-band weather radar located on top of Tai Mo Shan (3 km above sea level) for deriving the upper-air rain water content on rainy days.

The underlying principle of the variation minimization retrieval is similar to the variational assimilation method in NWP. An initial guess of the vertical profile for the retrieval is obtained from the 6-hour forecast of the regional numerical weather prediction system, Meso-NHM, run by the HKO. To speed up the convergence of the variational retrieval algorithm, the lowest 1500 m of the forecast profile from Meso-NHM was first calibrated based on the differences between the surface temperature forecasts by Meso-NHM and the temperatures measured by the automatic weather station (AWS). Such calibration often has insignificant effects on the retrieved profiles, but it speeds up the calculation by reducing the average number of iterations needed in the minimization process by providing a first-guess profile similar to the surface observations. Details on Meso-NHM can be found in Wong (2011).

3. Numerical schemes

The one-dimensional radiative transfer equation is given by

$$\frac{dI}{dx} = -\sum_i \rho_i(\sigma_i^a + \sigma_i^s)I + \sum_i \rho_i\sigma_i^a B(T_i) + \sum_i \rho_i\sigma_i^s J \tag{1}$$

where I is the intensity of the radiation, x is the optical path, i is a label for individual species of scattering/absorbing particles, $\sigma_i^a(\sigma_i^s)$ is the absorption (scattering) cross section of species i, ρ_i is the number density of species i, $B(T)$ is the Plank function at temperature T and J is a source function from scattering. J is related to scattering phase function $p(\Omega)$ by Eq. (2)

$$J = \int_\Omega p(\Omega)I(\Omega)d\Omega \tag{2}$$

Note that I, ρ_i, T and J are explicit functions of x, while σ_i^a and σ_i^s depend on x implicitly through their dependence on T.

Table 1
Frequencies and band widths of the 14-channel radiometer.

Channel	1	2	3	4	5	6	7
Frequency (GHz)	22.24	23.04	23.84	25.44	26.24	27.84	31.4
Band width (GHz)	0.23	0.23	0.23	0.23	0.23	0.23	0.23
Channel	8	9	10	11	12	13	14
Frequency (GHz)	51.26	52.28	53.86	54.94	56.66	57.30	58.00
Band width (GHz)	0.23	0.23	0.23	0.23	0.6	1	2

To solve Eq. (1), we discretize ρ_i and T along the optical path x. We first solve for I at these piecewise domains and join the domains together by requiring I to be continuous at the boundaries of the domains. Within the individual domains, we assume that the thermally emitted radiation is scattered no more than once, i.e.,

$$\rho_i J = \int_\Omega p(\Omega)B(T_i)d\Omega \tag{3}$$

As $p(\Omega)$ is integrated to unity, Eq. (3) further simplifies to

$$\rho_i J = B(T_i) \tag{4}$$

Thus, Eq. (1) simplifies to

$$\frac{dI}{dx} = -\sum_i \rho_i\sigma_i^e I + \sum_i \rho_i\sigma_i^e B(T_i) \tag{5}$$

where σ_i^e is the extinction cross section in individual domains.

The solution of Eq. (5) in the domain spanning x_j to x_{j+1} is

$$I(x_{j+1}) = \frac{\sum_k \Omega_k B(T_{kj})}{\sum_k \Omega_k}\left(1 - \exp\left(-\sum_i \Omega_i(x_{j+1}-x_j)\right)\right) + I(x_j)\exp\left(-\sum_i \Omega_i(x_{j+1}-x_j)\right) \tag{6}$$

where T_{kj} is the temperature in domain (x_j, x_{j+1}) for particle i and $\Omega_i = \rho_i\sigma_i^e$. In this study, we set $I(x_0) = 0$ because the radiometers operated by the HKO never point directly at the sun. Additionally, the radiometers operate at the microwave frequency, and the scattering of the solar-emitted microwave radiation by the atmosphere was negligible.

We assume that microwave radiation is absorbed by dry air (mainly oxygen and nitrogen molecules), water vapor, cloud water droplets and rain water droplets. Solid hydrometeors are not considered because they are not common in the study area in the period analyzed. Eq. (6) simplifies to

$$I(x_{j+1}) = B(T_j)\left(1 - \exp\left(-\sum_i \Omega_i(x_{j+1}-x_j)\right)\right) + I(x_j)\exp\left(-\sum_i \Omega_i(x_{j+1}-x_j)\right) \tag{7}$$

when there is a local thermal equilibrium in which the temperatures of all particles in the domain (x_j, x_{j+1}) are given by T_j. The assumption is valid when no rain is present. For rainy cases, we assume that the dry air, water vapor and cloud droplets are in a local thermal equilibrium, while the temperature of the rain droplets is computed from a microphysics scheme that is discussed later. σ_i^e for the gaseous components are obtained from Millimeter-wave Propagation Model (MPM-93) data (Liebe et al., 1993). σ_i^e from liquid water droplets is calculated using the formulas for Rayleigh scattering (for cloud droplets) and Mie scattering (for rain droplets), in which the empirical formula for the temperature and the frequency-dependent complex refractive index of bulk liquid water are the input.

The densities of O_2 and water vapor are determined using the ideal gas law and the mixing ratio, respectively. We assume that the number density of the cloud droplets is $N_c = 1 \times 10^8\,\mathrm{m}^{-3}$, in which the sizes follow a generalized gamma distribution, i.e.,

$$n_c(D) = N_c\frac{\alpha_c}{\Gamma(\nu_c)}\lambda_c^{\alpha_c\nu_c}D^{\alpha_c\nu_c-1}\exp(-(\lambda_c D)^{\alpha_c}) \tag{8}$$
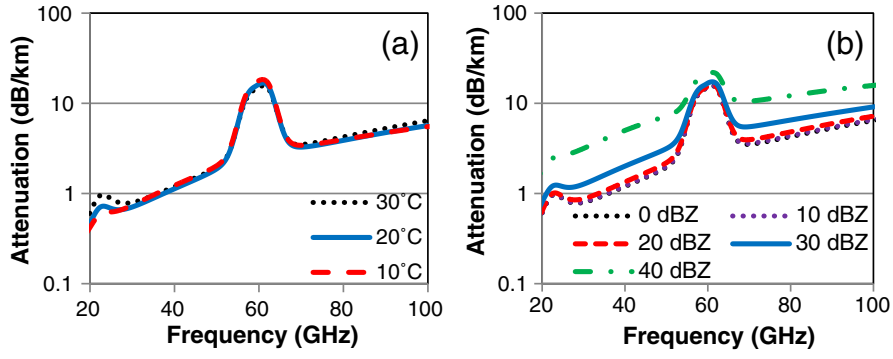
Fig. 1. (a) Attenuation rate of moist air at 1013 hPa, 100% relative humidity and 1 g m^{-3} liquid cloud droplets. The temperatures are 30 °C (dotted black curve), 20 °C (solid blue curve) and 10 °C (dashed red curve). (b) Attenuation rate of 30 °C moist air with rain droplets at 1013 hPa, 100% relative humidity, and 1 g m^{-3} liquid cloud droplets. The radar reflectivities of the rain droplets are 40 dBZ (dashed-dotted green curve), 30 dBZ (solid blue curve), 20 dBZ (dashed red curve), 10 dBZ (dotted purple curve) and 0 dBZ (dotted black curve). The last two curves nearly overlap.

where $\nu_c = 2$, $\alpha_c = 1$, D is the diameter of the droplet, and λ_c is the size parameter, which depends on the mixing ratio of the cloud water content. Such a distribution is also used in the Meso-NHM. Because the cloud water droplets are not single-sized, Ω_i is given by $\Omega_i = \int n_c(D)\sigma_i^e(D)dD$. For Rayleigh scattering,

$$\sigma_i^e = \frac{\pi}{24}k^4D^6\text{Re}\left((g)^2\right) + \frac{\pi kD^3}{2}\text{Im}\left(g\left[1 + \frac{k^2D^2}{60}(g)\frac{\varepsilon_w^2 + 27\varepsilon_w + 38}{2\varepsilon_w + 3}\right]\right) \tag{9}$$

where $g = \frac{\varepsilon_w - 1}{\varepsilon_w + 2}$, ε_w is the square of the frequency-dependent complex refractive index of bulk liquid water from Ray (1972), and k is the wavenumber from Bohren and Huffman (1998).

As mentioned, λ_c depends on the mixing ratio of the cloud water content. With $\nu_c = 2$ and $\alpha_c = 1$, the parameter can be expressed as

$$\lambda_c^3 = N_c\frac{10\pi\rho_w}{w_w\rho_a} \tag{10}$$

where ρ_w is the density of liquid water, w_w is the mixing ratio of liquid water, ρ_a is the density of the air. Additionally, from Eq. (9), Ω_i of the cloud water droplets is a linear combination of the 3rd, 5th and 6th moments of the size distribution. Numerically, the 3rd moment term contributes the most to σ_i^e, which is directly proportional to the volume fraction of the cloud water droplets.

We use a climatological diagnostic parameterization scheme for the mixing ratio of the cloud liquid water in this study. The scheme is that of Wang et al. (1995), which is based on relative humidity (RH):

$$\rho_l = w_w\rho_a = \begin{cases} 0.20 \text{ g m}^{-3} & \text{if RH} \geq 95\% \text{ and height} \leq 600 \text{ m} \\ 0.26 \text{ g m}^{-3} & \text{if RH} \geq 95\% \text{ and height} > 600 \text{ m} \end{cases} \tag{11}$$

The rain droplet size distribution is assumed to follow the Marshall–Parmer distribution:

$$N_r(D) = N_0e^{-\Lambda D} \tag{12}$$

$N_0 = 8000$ mm^{-1} m^{-3}, as shown in Sun and Crook (1997). The slope parameter Λ is derived from the radar reflectivity. Because the sizes of the raindrops are comparable to the operating wavelength of the radiometers, Mie theory is needed to evaluate σ_i^e. Similar to Bohren and Huffman (1998),

$$\sigma_i^e = \frac{2\pi}{k^2}\text{Re}\sum_{n=1}^{\infty}(2n+1)(a_n + b_n) \tag{13}$$

$$a_n = \frac{m\psi_n(mx)\psi'_n(x) - \psi'_n(mx)\psi_n(x)}{m\psi_n(mx)\xi'_n(x) - \psi'_n(mx)\xi_n(x)} \tag{14}$$

$$b_n = \frac{\psi_n(mx)\psi'_n(x) - m\psi'_n(mx)\psi_n(x)}{\psi_n(mx)\xi'_n(x) - m\psi'_n(mx)\xi_n(x)} \tag{15}$$

where $x = D\pi/\lambda$, m is the complex refractive index of liquid water, $\psi_n(x) = xj_n(x)$, $\xi_n(x) = xh_n(x)$, $j_n(x)$ and $h_n(x)$ are the spherical Bessel functions and spherical Hankel functions of the first kind, respectively. The numerical method for evaluating a_n and b_n can be found in Xu et al. (1999). The infinite sum in Eq. (13) is numerically replaced by a finite sum (up to N)

$$N = x + 4x^{\frac{1}{3}} + 2 \tag{16}$$

following Wiscombe's criterion (1980). For a 1 cm water droplet and 60 GHz microwave radiation, $x \approx 6.3$ and Eq. (16) indicates that a finite sum of no more than 20 terms is sufficient for our calculation. For numerical accuracy, the generation of $\psi_n(x)$ and $\xi_n(x)$ is initiated 20 orders higher than suggested by Eq. (16) because the computed σ_i^e is insensitive to a higher-generation starting order. The integral for evaluating the corresponding Ω_i is conducted using the 8-point Gaussian quadrature. At a reflectivity of 50 dBZ (corresponding to a rain rate of approximately 50 mm h^{-1} using the Marshall–Palmer relation), no more than a 5% difference was found between the attenuation coefficients calculated using the 8-point Gaussian quadrature and the 16-point Gaussian quadrature in the frequency regime. To outline the relative contribution of the individual components, the attenuation rates of various
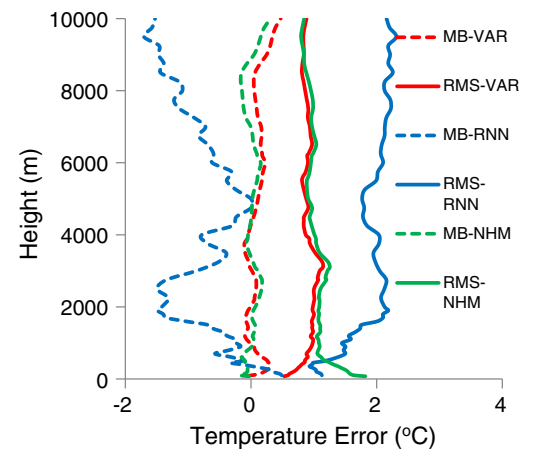

Fig. 2. Comparison of the performances in retrieving the temperature profiles. Please refer to the text for the abbreviation definitions.
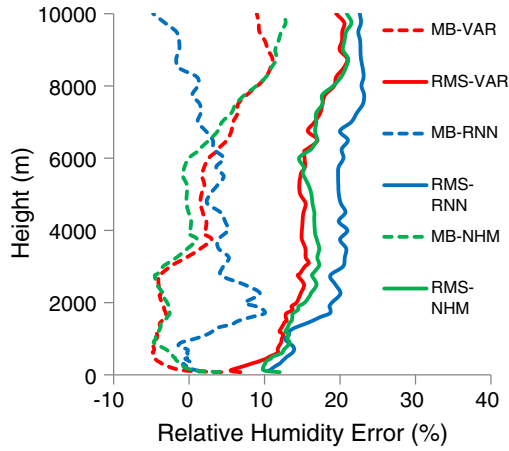
Fig. 3. Comparison of the performances in retrieving the relative humidity profiles.

configurations are shown in Fig. 1. The attenuation curves for different reflectivities overlap when the reflectivity is less than or equal to 10 dBZ. Hence, the extinction due to rain droplets is negligible if the radar reflectivity is less than 10 dBZ.

The radar reflectivity is generally height dependent due to interactions between individual droplets and interactions between droplets and the environment. In this study, we only explicitly consider the micro-physics of the evaporation of rain droplets as they fall into sub-saturated air. Because it is assumed that the size distribution of rain droplets always follows the Marshall–Parmer distribution, coalescence and breakup of rain droplets are implicitly considered by redistributing the rain water content among droplets of different sizes while preserving the total rain water content. However, coalescence between rain droplets and cloud droplets is not considered for simplicity. Details on the formulation of the evaporation of rain drops are discussed below.

For a rain drop of diameter D, the evolution of D over time t is given by

$$D\frac{dD}{dt} = \overline{f_v}\frac{4(R-1)}{\rho_w(A+B)} \tag{17}$$

where R is the relative humidity, $\overline{f_v}$ is the ventilation coefficient, $A = L_v^2/(k_a R_v T^2)$, $B = (\rho_{sv}(T)D_v)^{-1}$, L_v is the latent heat of evaporation of water, $\rho_{sv}(T)$ is the saturated vapor density at temperature T, k_a is the thermal conductivity of air and D_v is the diffusivity of water vapor in air, similar to Dudhia (1989) and Pruppacher and Klett (1997). Following Dudhia (1989), the fall speed of the rain is $V(D) = a(P_0/P)^{0.4}D^b$, where $a = 842$, $b = 0.8$, $P_0 = 1000$ hPa and P is the ambient pressure in hPa. The ventilation coefficient is parameterized by $\overline{f_v} = f_1 + f_2 Sc^{1/3}Re^{0.5}$, where $f_1 = 0.78$, $f_2 = 0.32$, Sc is the Schmidt number and Re is the Reynolds number. The evolution of the rain water content with height due to evaporation is given by

$$\frac{dm}{dz} = \int_0^\infty \frac{\pi\rho_w}{6V(D)}N(D)\frac{dD^3}{dt}dD \tag{18}$$
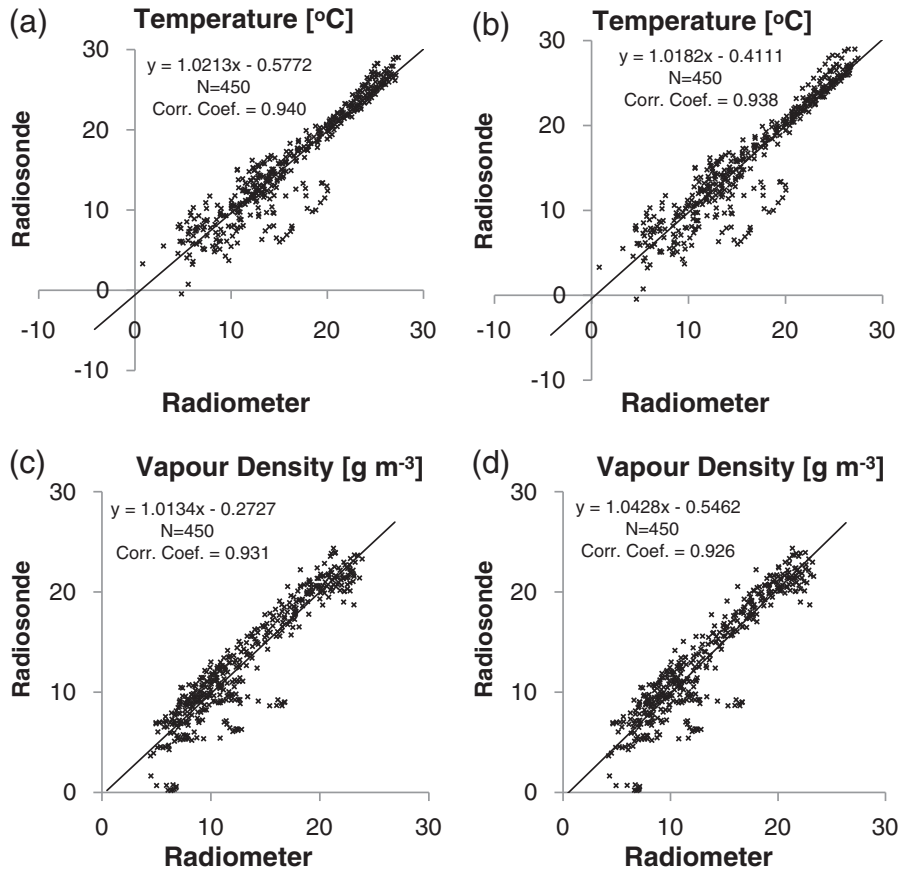

Fig. 4. Figure shows the correlation between the vertical temperature and vapor density profiles measured by the radiosonde and KP radiometer. The data are for 00 UTC and 12 UTC from May 2013 to April 2014 (excluding a 2-month period from late August to early October in 2013 due to the malfunction of the radiometer) during rainy conditions (radar reflectivity aloft ≥ 10 dBZ). For Fig. 4(a) and (c), the rain module is incorporated into the retrieval algorithm. For Fig. 4(b) and (d), there is no rain module in the retrieval algorithm. Only data 3000 m to sea level are plotted in the figure.
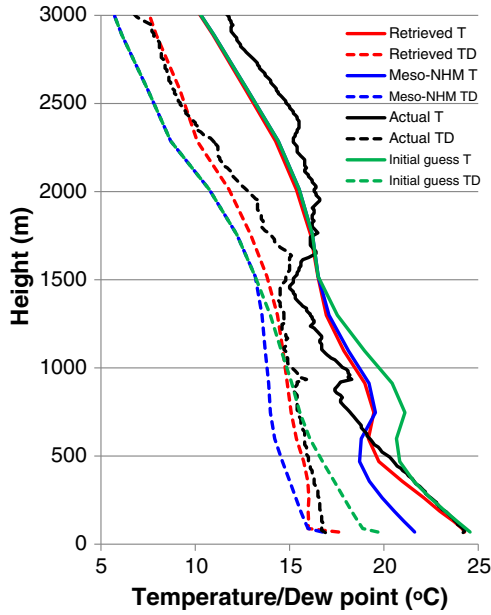
Fig. 5. Upper-air profiles at King's Park at 0000 UTC 21 October 2010. The black curves (solid for temperature, dashed for dew point) are those measured by the radiosonde and are taken as the ground truth. The 6-hour forecast from Meso-NHM is shown in blue. The green curves are the modified Meso-NHM profile (initial guess) using the surface AWS readings. The red curves are those retrieved with the algorithm discussed above.

where $N(D)$ is the size distribution of the droplets. By assuming that $N(D)$ follows the Marshall–Palmer distribution $N(D) = N_0 \exp(-\lambda D)$, Eq. (18) becomes

$$\frac{dm}{dz} = \frac{2\pi N_0 (R-1)}{A+B} \left[\left(\frac{P}{P_0}\right)^{0.4} \frac{f_1 \Gamma(2-b)}{a\lambda^{2-b}} + f_2 \left(\frac{P}{P_0}\right)^{0.2} Sc^{1/3} (a\nu_a)^{-0.5} \frac{\Gamma\left(\frac{5-b}{2}\right)}{\lambda^{\frac{5-b}{2}}} \right] \quad (19)$$

where ν_a is the kinematic viscosity of air. Note that λ is a function of m, so Eq. (19) is a differential equation that must be solved numerically. In
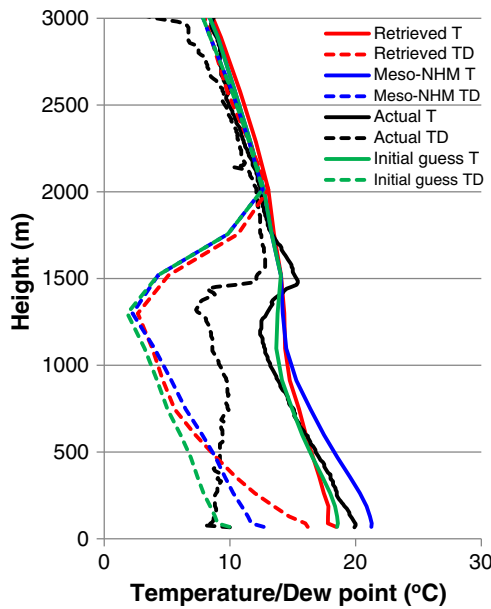

Fig. 6. Same as Fig. 5 except for 1200 UTC on 4 November 2010. Here, rain occurred, and the radar reflectivity above the radiosonde site and the radiometer site is 17 and 18 dBZ, respectively.

our retrieval algorithm, this vertical evolution of the rain water content is solved numerically by the mid-point method.

As water evaporates from the droplets, the temperature of the droplet becomes lower than the ambient temperature until equilibrium is reached. The equilibrium temperature of a droplet, which occurs within a few seconds, is approximately size independent (Pruppacher and Klett, 1997). The equilibrium temperature of the droplet is the solution to the following equation:

$$T = T_\infty - \frac{D_v L_v (\rho_{sv}(T) - \rho_v)}{k_a} \quad (20)$$

where T_∞ is the ambient temperature and ρ_v is the ambient vapor density. Eq. (20) is solved numerically by the false position method. For simplicity, we assume that the relaxation times are zero and that the droplets are always at their equilibrium temperatures.

The formulation above solves the one-dimensional radiative transfer equation for a given state of the atmosphere. For retrievals, however, we must find the state of the atmosphere given a set of observations using the one-dimensional variational approach (1DVAR). The cost function of the 1DVAR is

$$J\left(\overrightarrow{x}\right) = \left(H\left(\overrightarrow{x}\right) - \overrightarrow{y_0}\right)^T R^{-1} \left(H\left(\overrightarrow{x}\right) - \overrightarrow{y_0}\right) + \left(\overrightarrow{x} - \overrightarrow{x_0}\right)^T B^{-1} \left(\overrightarrow{x} - \overrightarrow{x_0}\right) \quad (21)$$

where $\overrightarrow{y_0}$ is the observation vector (composed of 14 brightness temperatures, the surface pressure, and the temperature and dew point measured by an AWS at the location of the radiosonde), $H\left(\overrightarrow{x}\right)$ is the observation operator, $\overrightarrow{x}$ is the state of the atmosphere (the pressures, temperatures and dew points at 50 vertical levels), $\overrightarrow{x_0}$ is the first guess by the model, R is the observation covariance matrix and B is the background error covariance matrix. B was obtained by the NMC method (Parrish and Derber, 1992, named for the National Meteorological Center, which is now the National Centers for Environmental Prediction) using model data over a 1-year period. R is derived from the difference between the actual observations measured by the HKIA radiometer and the simulated observations using $H\left(\overrightarrow{x}\right)$, in which the vertical profile is measured by the radiosonde at King's Park from Sept 2008 to Aug 2010. Because the HKIA radiometer is located 26 km away from the radiosonde site, it is possible that the weather conditions differ, particularly during rain. Hence, only data in those two years that satisfy the following conditions are included in the training dataset: (a) the difference in the radar reflectivity aloft between the radiometer and the radiosonde is no more than 10 dBZ; or (b) the reflectivity at both sites is smaller than 10 dBZ. This calculation of the R matrix handles the difference in locations between the radiosonde and radiometer. $J\left(\overrightarrow{x}\right)$ is minimized using the Broyden–Fletcher–Goldfarb–Shanno (BFGS) scheme (Fletcher, 2000) with the Jacobian $\nabla_x J\left(\overrightarrow{x}\right)$, which is computed using a "brute force" approach, i.e., by perturbing the individual components of $\overrightarrow{x}$ by 1 hPa (or 1 °C).

For the studies that use the KP radiometer data, the same R matrix is applied. Because the KP radiometer is quite new, we do not have enough data to re-calculate the R matrix for the retrieval algorithm.

4. Retrieval results

The existing retrieval method in use at the HKO is based on neural networks (Chan, 2010). The temperature profile from the current retrieval method is not accurate enough for nowcasting convective development due to the overestimated instability caused by a
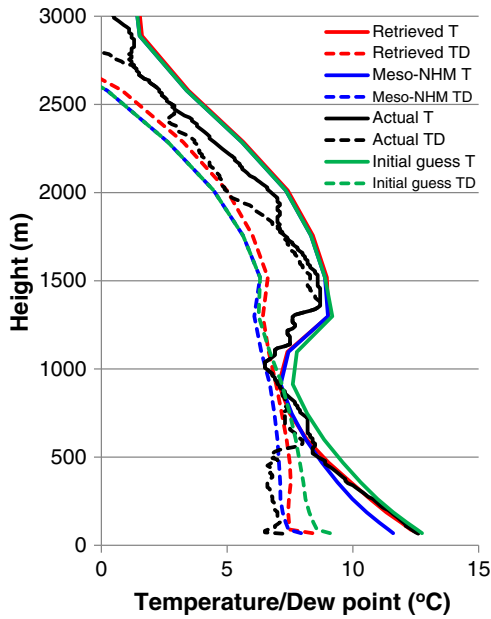
Fig. 7. Same as Fig. 5 except for 0000 UTC on 12 February 2011.

warm bias in the low levels and a cold bias aloft. The purpose of the development of the retrieval method discussed above is to improve the performance of the vertical profile retrieval and to facilitate

nowcasting convective development by incorporating more accurate vertical profiles.

4.1. Comparison with the existing retrieval method

Figs. 2–3 present a comparison of the performances in retrieving the temperature and humidity profiles between the existing neural net-work method (RNN) and the variational retrieval method (VAR) of the HKIA radiometer. The heights in the figures and the discussion below reference sea level. Because the initial estimation of the profiles is from the 6-hour forecast profile of Meso-NHM (NHM hereafter), the model's performance is also shown in Figs. 2–3 for comparison. Mean error, or bias, (MB) and root-mean-squared error (RMSE) are used as the metrics for the comparisons.

It is clear from Figs. 2–3 that, among the three methods, the VAR method produces the most accurate profiles (in terms of temperature and relative humidity). Additionally, Meso-NHM provides a rather accu-rate middle to high upper-air profile with the VAR method. The VAR method uses the brightness temperatures and the readings from the AWS to improve the accuracy of the lower level of the retrieved profiles. By combining the strength of the model, i.e., the highly accurate upper-air profiles, with the measurement from the radiometer, which effec-tively captures the near-surface conditions, VAR outperforms both RNN and NHM.

A comparison of our VAR results with other statistical retrieval methods used in studies near Hong Kong leads to similar conclusions for temperature. For example, Tan et al.'s retrieval method, which com-bines principal component analysis and stepwise regression (PSR), pro-vides root-mean-squared errors of no less than 1 °C for the temperature in the lowest 2000 m of the profile and of approximately 1.5 °C above
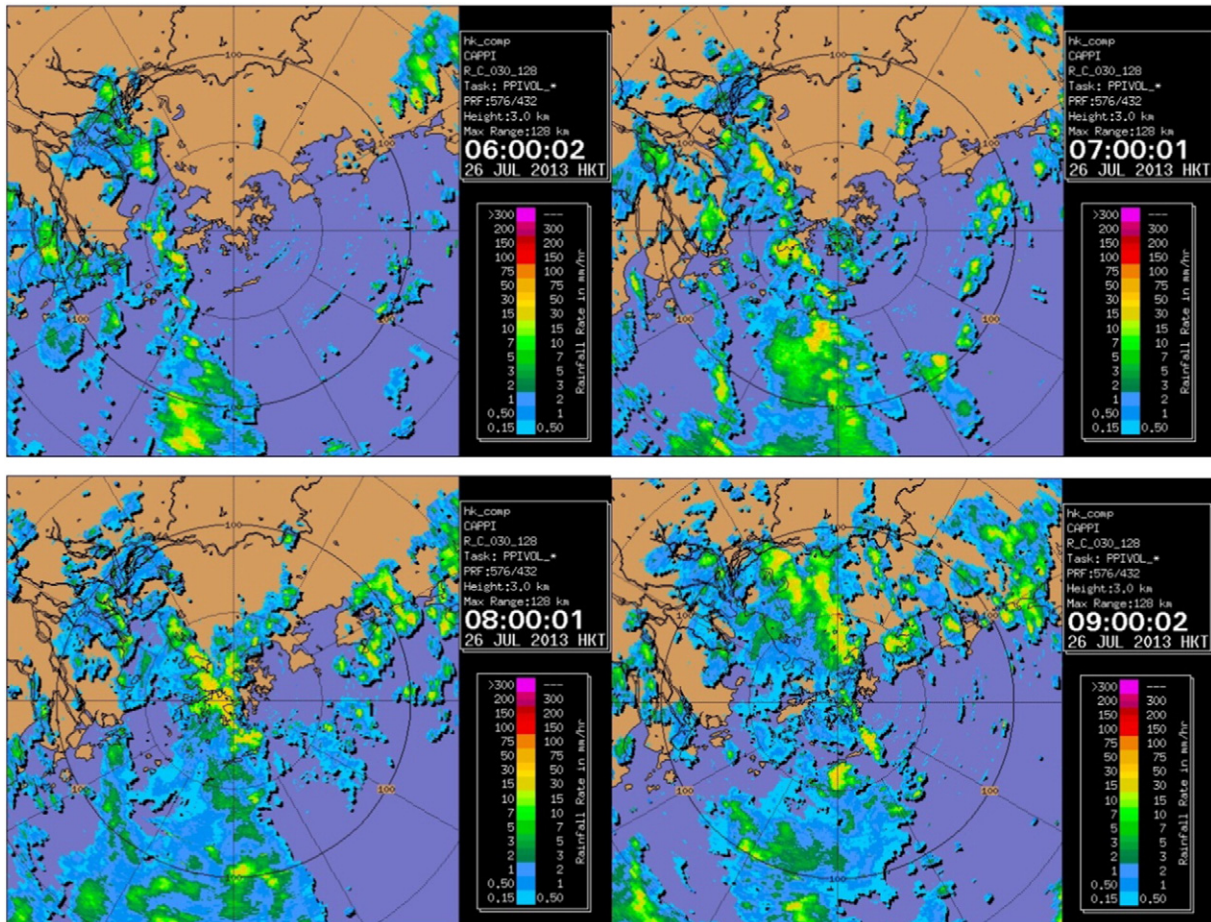

Fig. 8. Shows the radar sequence illustrating the evolution of the convective systems across Hong Kong on the morning of 26 July 2013. Hong Kong Time (HKT) is 8 h ahead of UTC.
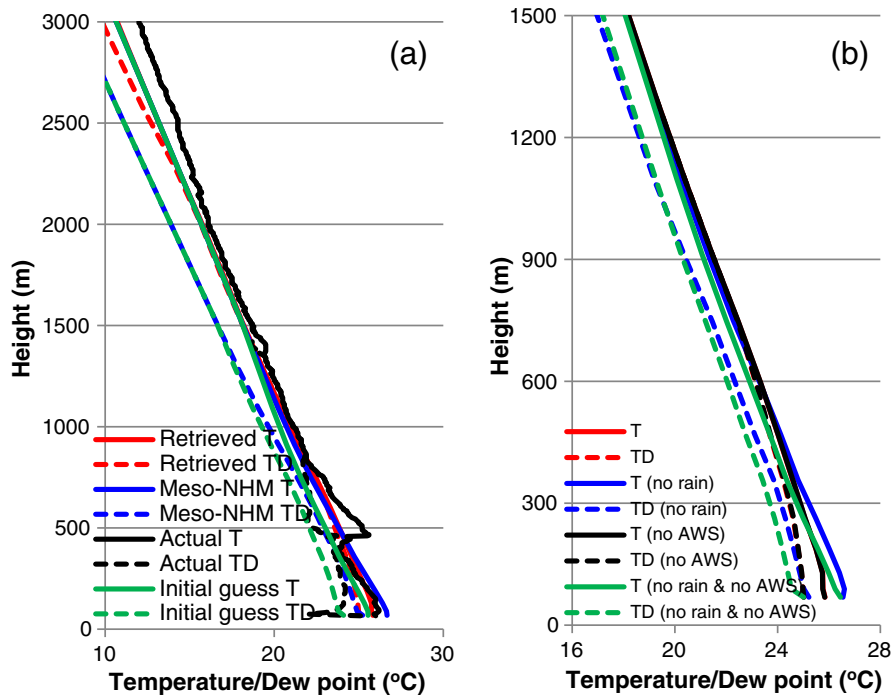
Fig. 9. (a) Same as Fig. 5 except for 0000 UTC on 26 July 2013. The reflectivity above King's Park is 43.5 dBZ. Compared with both the model forecast profile and the first guess, the retrieved profile provides the most accurate temperature profile for the lowest 500 m. (b) Comparisons between the retrieved profile obtained with different configurations. The red curves (over-lapping with the black curve in this case) are the same as in (a). Black: same as red except the first guess profile is not corrected by the surface AWS readings before conducting the var-iational retrieval (no AWS). Green (blue): same as red (black), except the rain module is turned off in the retrieval (no rain).

(Fig. 5 of Tan et al., 2011). Compared with the VAR results of no more than 1 °C in the lowest 2000 m and approximately 1 °C above, VAR is more accurate in retrieving temperature profiles than PSR. The results shown in Fig. 2 also suggest that, except for the lowest 1000 m, the tem-perature profiles from NHM are more accurate than those of PSR. The profiles from VAR inherited the skills from NHM and performed better than PSR in retrieving the temperature profiles. Note that although the radiometer in Tan et al. is farther from the KP radiosonde site than the HKIA radiometer (77 km versus 26 km), it also has more channels than the HKIA radiometer (35 channels compared with 14 channels). The extra microwave channels may partially offset the additional errors caused by the greater spatial distance from the radiosonde site. Because of the greater spatial variation in the moisture content, we do not com-pare the performances in retrieving vapor density profiles.

4.2. Significance of the rain module in the retrieval algorithm

To demonstrate the impact of adding the rain module to the retrieval algorithm, we compare the vertical profiles of temperature and vapor density obtained from the retrieval algorithm with vertical profiles measured by the radiosonde. Because the contribution from rain water is negligible for a radar reflectivity of less than 10 dBZ, we only compare those data obtained when the radar reflectivity is larger than

Table 2
Comparison of the instability indices retrieved by different algorithms.

Instability indices	K index (K)	Total totals index (K)	CAPE (J/kg)	Total precipitable water (mm)
Actual (radiosonde)	40.1	42.8	1802.8	70.6
Radiometer (neural network retrieval)	42.9	47	1100.9	73.9
Radiometer (1D-var)	39	44	2086	70

or equal to 10 dBZ. As suggested by the results shown in Figs. 2 and 3, the comparison focuses on the lowest 3000 m of the profiles.

The correlation between the vertical profiles measured by the radio-sonde and those retrieved by the radiometer is shown in Fig. 4. Two sets of figures (Fig. 4(a) and (c) versus Fig. 4(b) and (d)) are shown, and the difference between them is the presence/absence of the rain module in the retrieval algorithm. The results shown in Fig. 4 suggest that there is a higher correlation between the vertical profiles measured by the radio-sonde and the radiometer for both the temperature and vapor density when the rain module is incorporated into the retrieval algorithm. The rain water content increases the attenuation rate of microwave radia-tion of the air. Because the temperature usually decreases with increas-ing height in the troposphere, the presence of rain water further attenuates the microwave radiation emitted from the upper tropo-sphere and increases the emission of microwave radiation in the lower troposphere. Hence, the rain water content tends to increase the brightness temperature measured by the radiometer. If there is no rain module in the retrieval algorithm, then the simulated brightness temperature would be far too low compared with the observations. It would be difficult for the minimization algorithm to improve the verti-cal profiles beyond the initial guess (an example to illustrate this is pro-vided later). Hence, the correlation between the retrieved and the actual profiles is weak.

4.3. Examples of retrieved profiles

Four retrieved profiles (0000 UTC on 21 October 2010, 1200 UTC on 4 November 2010, 0000 UTC on 19 November 2010 and 0000 UTC on 26 July 2013) are discussed below as examples. Each profile shows a differ-ent aspect of the profile retrieval.

Fig. 5 shows the profiles from 0000 UTC on 21 October 2010 over King's Park. The profile measured by the radiosonde (black curves) shows a dry low level with a shallow temperature inversion near

1000 m. The forecast profile from Meso-NHM (blue curves) manages to capture the temperature inversion, but the inversion is too low and deep. The surface temperature from Meso-NHM is too low compared with the actual profile. After calibrating the lowest 1500 m of the profile using the AWS data (green curves), the negative bias of the temperature near the surface was corrected but a significant warm bias occurs in the 500 m to 1000 m height interval because the temperature inversion is too low and deep in the forecast profile. The variational retrieval algorithm (profile shown in red) corrects this warm bias and produces a more accurate profile compared with the blue and green curves. The algorithm also slightly corrects the dry bias at approximately 1500 m in the Meso-NHM profiles. If the blue curves are used as the first guess in the variational retrieval algorithm, then the resultant profile is the same as the red profile. The minimization result is insensitive to the initial guess in this case.

Fig. 6 shows the profile retrieved in rainy conditions (1200 UTC on 4 November 2010). The radar reflectivity recorded at King's Park, the radiosonde site, and at the radiometer site are 17 and 18 dBZ, respectively. The radiosonde profile is moist at the 2000–3000 m level but dry below. The forecast temperature profile from Meso-NHM is quite accurate. There is a slight warm bias in the lowest 1500 m of the temperature profile. The forecast humidity profile is too dry in the lowest 2000 m. After modification using the AWS reading, the dew point profile is further underestimated. The retrieval algorithm in this case manages to correct the dry bias in the low levels, although the correction is not sufficient.

Fig. 7 shows the performance of the retrieval algorithm in analyzing a low-level inversion layer at 0000 UTC on 12 February 2011. A northeast winter monsoon formed a low-level inversion. Meso-NHM is able to forecast the presence of the inversion, but the surface temperature forecast by Meso-NHM is too low. After modifying the Meso-NHM vertical profile with the AWS data, the lowest part of the profile is corrected, but the modification results in a warm bias in the 500–1000 m layer. Our retrieval algorithm corrected this warm bias and provided the best results among the three methods.

The last example illustrates the value of the retrieval algorithm for nowcasting convective development. A low-pressure trough lingered around the coastal area of Guangdong on 26 July 2013. Convective systems swept across Hong Kong during the day, as illustrated by the radar sequence shown in Fig. 8. At 0000 UTC on 26 July 2013, the radar reflectivity over King's Park was 43.5 dBZ during rainy conditions. Vertical profiles retrieved with the KP radiometer, along with the initial guess from Meso-NHM and the actual profile from the radiosonde, are shown in Fig. 9(a). Again, our retrieval algorithm improves the initial guess of Meso-NHM and produces vertical profiles that are similar to those of the radiosonde. The instability indices computed from our retrieval algorithm are also closer to those derived from the radiosonde than those obtained using the neural network retrieval algorithm, as shown in Table 2.

This example also illustrates how the rain module helps produce a more accurate vertical profile. The results shown in Fig. 9(b) suggest that the retrieved profile has very little dependence on the first guess of the retrieval process when the rain module is incorporated into the retrieval algorithm. However, if there is no rain module, the results are very different, depending on whether the model forecast profile is first corrected by the reading from the surface AWS. As discussed above, the simulated brightness temperature would be far too low if the attenuation of microwave radiation by rain water is neglected in the calculation. This cold bias in the brightness temperature is the dominant component in the cost function for the minimization algorithm. Hence, the minimization algorithm is ineffective for improving the vertical profile beyond the initial guess; this initial-guess-dependent result is shown in Fig. 9(b).

5. Conclusion

By comparing the vertical profiles retrieved from various algorithms with the actual vertical profile measured at the KP radiosonde site, we find that the variational retrieval algorithm performs better than the statistical algorithm. We also find that the incorporation of warm-rain microphysics is essential to the performance of the retrieval algorithm under rainy conditions. The instability indices derived from the retrieved profile using the variational algorithm are more realistic than those of other methods. The variational algorithm has potential for nowcasting convective initiation. Further studies are needed to evaluate the usefulness of more sophisticated rain microphysics in the performance of retrieval algorithms.

Acknowledgments

References

Adams, D.K., Souza, E.P., 2009. CAPE and convective events in the southwest during the North American Monsoon. Mon. Weather Rev. 137, 83–98.

Bohren, C.F., Huffman, D.R., 1998. Absorption and Scattering of Light by Small Particles. John Wiley & Sons, Inc. (530 pp.).

Cadeddu, M.P., Liljegren, J.C., Turner, D.D., 2013. The Atmospheric radiation measurement (ARM) program network of microwave radiometers: instrumentation, data and retrievals. Atmos. Meas. Tech. 6, 2359–2372.

Chan, P.W., 2009a. Performance and application of a multi-wavelength, ground-based microwave radiometer in intense convective weather. Meteorol. Z. 18, 253–265.

Chan, P.W., 2009b. Nowcasting Applications of a Microwave Radiometer in Hong Kong. 8th International Symposium on Tropospheric Profiling: Integration of Needs, Technologies and Applications, Delft, The Netherlands.

Chan, P.W., 2010. The Use of Neural Network Retrieval for Thermodynamic Profiles of a Ground-based Microwave Radiometer. The 11th Specialist Meeting on Microwave Radiometry and Remote Sensing of the Environment, Washington, DC, USA.

Cimini, D., Campos, E., Ware, R., Albers, S., Giuliani, G., Oreamuno, J., Joe, P., Koch, S.E., Cober, S., Westwater, E., 2011. Thermodynamic atmospheric profiling during the 2010 Winter Olympics using ground-based microwave radiometry. IEEE Trans. Geosci. Remote Sens. 49, 4959–4969.

Dudhia, J., 1989. Numerical study of convection observed during the winter monsoon experiment using a mesoscale two-dimensional model. J. Atmos. Sci. 46, 3077–3107.

Fernández-González, S., Valero, F., Sanchez, J.L., Gascon, E., Lopez, L., Garcia-Ortega, E., Merino, A., 2014. Observation of a freezing drizzle episode: a case study. Atmos. Res. 149, 244–254.

Fletcher, R., 2000. Practical Method of Optimization. 2nd edition. John Wiley & Sons, Inc. (456 pp.).

Hewison, T.J., 2007. 1D-VAR retrieval of temperature and humidity profiles from a ground-based microwave radiometer. IEEE Trans. Geosci. Remote Sens. 45, 2163–2168.

Liebe, H.J., Hufford, G.A., Cotton, M.G., 1993. Propagation modeling of moist air and suspended water/ice particles at frequency below 1000 GHz. Proc. NATO/AGARD Wave Propagation Panel, 52nd meeting, No. 3/1–10, Mallorca, Spain.

Lin, P.F., Chang, P.L., Jou, B.J.D., Wilson, J.W., Roberts, R.D., 2011. Warm season afternoon thunderstorm characteristic under weak synoptic-scale forcing over Taiwan Island. Weather Forecast. 26, 44–60.

Lin, P.F., Chang, P.L., Jou, B.J.D., Wilson, J.W., Roberts, R.D., 2012. Objective prediction of warm season afternoon thunderstorms in Northern Taiwan using a fuzzy logic approach. Weather Forecast. 27, 1178–1197.

Parrish, D.F., Derber, J.C., 1992. The National Meteorological Center's spectral statistical-interpolation analysis system. Mon. Weather Rev. 120, 1747–1763.

Pruppacher, H.R., Klett, J.D., 1997. Microphysics of Clouds and Precipitation. Kluwer Academic Publishers (954 pp.).

Ray, P.S., 1972. Broadband complex refractive indices of ice and water. Appl. Opt. 11, 1836–1844.

Sun, J., Crook, N.A., 1997. Dynamical and microphysical retrieval from Doppler radar observations using a cloud model and its adjoint: Part I. model development and simulated data experiments. J. Atmos. Sci. 54, 1642–1661.

Sun, J., Chen, M., Wang, Y., 2010. A frequent-updating analysis system based on radar, surface and mesoscale model data for the Beijing 2008 Forecast Demonstration Project. Weather Forecast. 25, 1715–1735.

Tan, H., Mao, J., Chen, H., Chan, P.W., Wu, D., Li, F., Deng, T., 2011. A study of a retrieval method for temperature and humidity profiles from microwave radiometer observations based on principal component analysis and stepwise regression. J. Atmos. Ocean. Technol. 28, 378–389.

Wang, Z., Xu, P., Deng, J., Yan, W., 1995. Simulation of atmospheric vapor, liquid water content, and excess propagation path length based on a 3-channel microwave radiometer sensings (in Chinese). J. Nanjing Inst. Meteor. 18, 396–403.

Wiscombe, W.J., 1980. Improved Mie scattering algorithms. Appl. Opt. 19, 1505.

Wong, W.K., 2011. Development of Operational Rapid Update Non-hydrostatic NWP and Data Assimilation Systems in the Hong Kong Observatory. Technical Reports of the Meteorological Research Institute No. 65: "International Research for Prevention and Mitigation of Meteorological Disasters in Southeast Asia", pp. 87–100.

Wong, W.K., Yeung, L.H.Y., Wang, Y.C., Chen, M., 2009. Towards the Blending of NWP with Nowcast—Operation Experience in B08FDP. WMO Symposium on Nowcasting, Whistler, B.C. Canada.

Woods, C.P., Stoelinga, M.T., Locatelli, J.D., Hobbs, P.V., 2005. Microphysical processes and synergistic interaction between frontal and orographic forcing of precipitation during the 13 December 2001 IMPROVE-2 event over the Oregon Cascades. J. Atmos. Sci. 62 (10), 3493–3519.

Xu, Y., Gustafson, B.A.S., Giovane, F., Blum, J., Tehranian, S., 1999. Calculation of the heat-source function in photophoresis of aggregated spheres. Phys. Rev. E 60, 2347–2365.

Xu, G., Ware, R., Zhang, W., Feng, G., 2014. Effect of the off-zenith observation on reducing the impact of precipitation on ground-based microwave radiometer measurement accuracy in Wuhan. Atmos. Res. 140–141, 85–94.

Yeung, H.Y., Wong, W.K., Chan, K.Y., Lai, S.T., 2009. Applications of Hong Kong Observatory Nowcasting System Swirls-2 in Support of the 2008 Beijing Olympic Games. WMO Symposium on Nowcasting, Whistler, B.C. Canada.